IOPscience iopscience.iop.org

Home Search Collections Journals About Contact us My IOPscience

Stabilizing effect of resistivity towards ELM-free H-mode discharge in lithium-conditioned NSTX

This content has been downloaded from IOPscience. Please scroll down to see the full text.

View the table of contents for this issue, or go to the journal homepage for more

Download details:

IP Address: 198.125.231.54
This content was downloaded on 18/07/2017 at 20:44

Please note that terms and conditions apply.

You may also be interested in:

The effect of progressively increasing lithium coatings on plasma discharge characteristics, transport, edge profiles and ELM stability in the National Spherical Torus Experiment
R. Maingi, D.P. Boyle, J.M. Canik et al.

Enhanced confinement scenarios without large edge localized modes in tokamaks: control, performance, and extrapolability issues for ITER
R. Maingi

Advances in H-mode physics for long-pulse operation on EAST
Baonian Wan, Jiangang Li, Houyang Guo et al.

Enhanced H-mode pedestals with lithium injection in DIII-D
T.H. Osborne, G.L. Jackson, Z. Yan et al.

The relationships between ELM suppression, pedestal profiles and lithium wall coatings in NSTX
D P Boyle, R Maingi, P B Snyder et al.

Chapter 2: Plasma confinement and transport
E.J. Doyle (Chair Transport Physics), W.A. Houlberg (Chair Confinement Database and Modelling), Y. Kamada (Chair Pedestal and Edge) et al.

Modelling of ELM dynamics for DIII-D and ITER
A Y Pankin, G Bateman, D P Brennan et al.

Linear peeling–ballooning mode simulations in snowflake-like divertor configuration using BOUT++ code
J.F. Ma, X.Q. Xu and B.D. Dudson

IOP Publishing | International Atomic Energy Agency Nuclear Fusion

Nucl. Fusion **57** (2017) 076005 (11pp) https://doi.org/10.1088/1741-4326/aa6b25

Stabilizing effect of resistivity towards ELM-free H-mode discharge in lithium-conditioned NSTX

Debabrata Banerjee[1], **Ping Zhu**[1,2] **and Rajesh Maingi**[3]

[1] CAS Key Laboratory of Geospace Environment and Department of Modern Physics, University of Science and Technology of China, Hefei, Anhui 230026, People's Republic of China
[2] Department of Engineering Physics, University of Wisconsin-Madison, Madison, WI 53706, United States of America
[3] Princeton Plasma Physics Laboratory, PO Box 451, Princeton, NJ 08543, United States of America

E-mail: pzhu@ustc.edu.cn

Received 21 November 2016, revised 19 March 2017
Accepted for publication 4 April 2017
Published 12 May 2017

Abstract

Linear stability analysis of the national spherical torus experiment (NSTX) Li-conditioned ELM-free H-mode equilibria is carried out in the context of the extended magneto-hydrodynamic (MHD) model in NIMROD. The purpose is to investigate the physical cause behind edge localized mode (ELM) suppression in experiment after the Li-coating of the divertor and the first wall of the NSTX tokamak. Besides ideal MHD modeling, including finite-Larmor radius effect and two-fluid Hall and electron diamagnetic drift contributions, a non-ideal resistivity model is employed, taking into account the increase of Z_{eff} after Li-conditioning in ELM-free H-mode. Unlike an earlier conclusion from an eigenvalue code analysis of these equilibria, NIMROD results find that after reduced recycling from divertor plates, profile modification is necessary but insufficient to explain the mechanism behind complete ELMs suppression in ideal two-fluid MHD. After considering the higher plasma resistivity due to higher Z_{eff}, the complete stabilization could be explained. A thorough analysis of both pre-lithium ELMy and with-lithium ELM-free cases using ideal and non-ideal MHD models is presented, after accurately including a vacuum-like cold halo region in NIMROD to investigate ELMs.

Keywords: Li-conditioned ELM-free H-mode, resistive stabilization, Z_{eff}, NIMROD, NSTX

(Some figures may appear in colour only in the online journal)

1. Introduction

It has been predicted that high pedestal top pressure in the high confinement discharge mode (H-mode) at the international thermonuclear experimental reactor (ITER) can assist increases in the fusion power gain [1]. However, the associated steep gradient of the pedestal pressure profile effectively acts as a driving force that can trigger pressure-driven ballooning modes localised at the edge pedestal. A high bootstrap current fraction has been proposed to facilitate nearly non-inductive operation of ITER; but this would induce a highly peaked edge-current profile being able to excite the current-driven peeling modes. Further, periodic bursts of type-I edge localised modes (ELMs) are believed to be generated in the nonlinear phase of the coupled peeling-ballooning modes, localised at the edge pedestal [2–4]. A substantial amount of plasma-stored energy is carried away by these periodic ELMs to outside of the confined domain, actively causing deterioration of the plasma facing components (PFCs) along with heat and particle depositions. Overall, mitigation and suppression of these ELMs is essential for maintaining long-duration steady state operation of H-mode discharge in fusion reactors. Recently, H-mode discharges in NSTX have been successfully achieved with partial to complete avoidance of ELMs,

 © 2017 IAEA, Vienna Printed in the UK

following Li conditioning of the PFCs. These achievements will remain influential in the context of successful operation of next-generation fusion reactors such as ITER [5] and the China fusion engineering test reactor (CFETR) [6], provided the NSTX physics could be extrapolated.

As an approach to ELM mitigation and suppression, experiments with externally seeded Li species have been conducted in different tokamaks, e.g. NSTX, EAST and DIII-D. Since 2008, NSTX has been consistently operated in the H-mode regime following application of Li coatings on the graphite PFCs. With high Li levels of pre-discharge evaporation, completely ELM-free H-mode discharges have been achieved [7, 8]. In addition, combined methods of prior discharge coatings and real-time Li injection have been used on EAST to obtain ~20 s ELM-free discharge [9]. On DIII-D, real-time Li evaporation has been found to be successful as a means of achieving short-duration regimes with very low ELM frequency and improved performance [10]. Apart from Li, other low-Z impurities are also routinely seeded in different machines to improve the pedestal height. In JET, the nitrogen seeding helps to increase pedestal height with ITER like Be/W wall [11]. However, ELMs have also been found to assist the flushing of intrinsic core impurities outside of the plasma domain, significantly reducing unnecessary impurity accumulation. Therefore, the present strategy is to efficiently control the ELM size and frequency so as to maintain ELMs that are within the beneficial limit for a fusion reactor. For example, for the purpose of ELM control by mitigating the ELM size, Li-granule-injected ELM-pacing has recently been investigated in the DIII-D experiment [12]. The initial success of this approach to ELM control has revealed the necessity for exploration of the mechanism behind the observed suppression, so that this technique can be further improved in future experiments. Various effects have been observed in experiments following Li conditioning towards ELM suppression, such as pedestal profile modification, increased radiation levels and increases in the effective charge number Z_{eff}. A previous analysis using the ideal magneto-hydrodynamic (MHD) eigenvalue code ELITE [7, 13], has shown the possible complete stabilising role of profile modification. Our analysis based on a two-fluid MHD model in the initial value code NIMROD indicates that low-n modes remain unstable in spite of the profile modification effect. So, contrary to the previous result [13], linear stability analysis in NIMROD indicates that profile modification alone after Li conditioning is necessary, but may be insufficient to explain complete stabilisation. Therefore, the changes responsible for ELM suppression and their mechanism are not completely understood. This article presents a probable answer to this question in the context of the NSTX ELM mitigation experiment on the basis of the extended MHD model.

We have focused on understanding the physical mechanism behind ELM suppression at the national spherical torus experiment (NSTX). The extended MHD-principle-based initial-value code NIMROD is employed for numerical calculation of the NSTX ELM-suppressed experimental data. In our NIMROD calculation, using NSTX equilibrium profiles, a new kind of stabilisation of low-n peeling-ballooning modes due to enhanced resistivity is identified. This finding constitutes a consistent explanation of the ELM suppression phenomenon in NSTX. The primary result of this new finding of resistive stabilisation has been reported briefly in a recent brief communication [14]. In this article, the complete analyses are presented, based on both the ideal single- and two-fluid MHD models, and the two-fluid resistive MHD model using a Spitzer resistivity profile for a thorough comparison of the pre-lithium ELMy reference and with-lithium ELM-free H-mode cases. The resistivity profile effect on the stabilisation of low-n ELMs is also determined from the difference between the results obtained using constant and Spitzer resistivity profiles in the NIMROD calculation.

The remainder of this article is organised as follows: First, a short description of the results of the NSTX Li-coating experiment is presented in the next section, including information on the equilibrium profiles used in our simulation. In the third section, the extended MHD equations in NIMROD is briefly introduced. Then, the results of the linear stability analyses of the pre- and with-lithium equilibrium profiles are described in the fourth and fifth sections, respectively. In the sixth section, comparisons are drawn between these two cases. In the final section, the results are summarised and discussed.

2. NSTX lithium-coated experiments and related equilibria

The low aspect ratio (~1.3) highly triangular shaped plasma of symmetric double null diverted configuration of NSTX usually achieves higher normalized beta value ~5–6.5 [15] with the highest one 7.2 (in $m.T\ \mathrm{MA}^{-1}$) [16]. Like higher aspect ratio tokamaks, NSTX also has routinely observed a wide variety of ELMs including type-I ELMs with magnitude $\Delta W/W \sim 2-15\%$ (ratio of energy loss due to each ELM to the stored plasma energy), type-III ELMs with stored energy loss fraction between 2–5% [17] and small type-V ELMs [18]. Although numerical edge stability calculations following the peeling-ballooning model have predicted access to a higher pedestal gradient and height in NSTX than higher aspect ratio tokamaks with the opening of second stability regimes [19], a higher pedestal pressure without any Li conditioning has not been found. In the first campaign of 2008 (shots #129015–129041), after progressively increasing lithium (Li) coatings on the divertor and the first wall of NSTX, a completely ELM-free H-mode was achieved for a duration of ~0.8 s in shot #129038; this was reproduced in subsequent experiments. Lithium evaporation was first applied prior to shot #129021, so that the early discharges (e.g. #129015, used in our simulation as a reference ELMy case) were fully Li-free boronized shots. The ELMs in these discharges belong to ordinary type-I classification with fractional energy drop (2–5)% and nominal frequency 100 Hz after NBI heating of 4 MW [8]. The comparative results shown in this article, are obtained after analyzing magneto-hydrodynamic (MHD) stability of the reference boronized ELMy shot #129015 and lithiated ELM-free shot #1209038. The description of the experimental technique of Li-conditioning and subsequent results are documented in detail in many recent articles

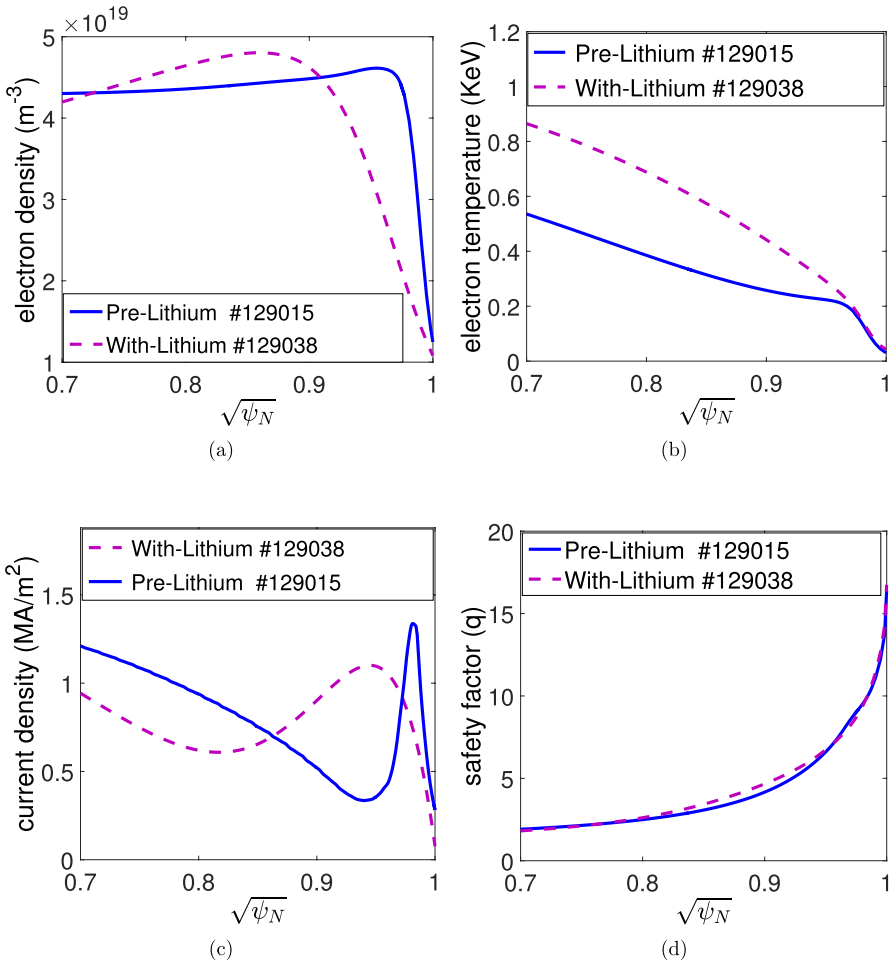

Figure 1. Radial profiles of electron density (*a*), electron temperature (*b*), current density (*c*) and safety factor (*d*) of NSTX ELM experiments. Blue solid line corresponds to pre-lithium ELMy-discharge and red dotted line to the with-lithium ELM-free discharge. ψ_N is the normalized poloidal flux function. The pedestal top position of electron density profile has moved far inward in with-lithium case (red) compared to the pre-lithium profile (blue). The gradient near to the edge in temperature profile remains unchanged but within 95% of ψ_N, a substantial change has occurred. The highly peaked bootstrap region in edge current density (*c*) in pre-lithium case (blue line), becomes more widened in with-lithium case (red line). However, the safety factor profile (*d*) is almost unchanged.

[8, 20–22]. In brief, after the Li-coating thickness was gradually enhanced, the recycling gradually decreased as Li has high chemical affinity with atomic hydrogen isotopes. As a result, an 80% reduction of divertor D_α signals was observed in the shot #129038, with no ELM-like spikes. Plasma stored energy and normalized peak β_N are almost at the same level, although the NBI power was reduced from 4 MW to 2 MW in the lithiated discharge. The normalized energy confinement time in the ELM-free shot was increased by ∼50% above the reference one. With reduction of ELMs, the value of $Z_{\rm eff}$ at the pedestal was increased upto a value of 4 (twice than the reference shot) [20, 21].

The reduced recycling from the divertor plates following Li coating reduces the edge electron density in the scrape-off layer and near the separatrix region. While the particle and thermal transport increase slightly near the separatrix, they are reduced substantially in the vicinity of the H-mode pedestal. The pedestal profiles of the electron density, temperature and electron pressure are thus altered. As shown in figure 1(*a*), the pedestal top position of the electron density profile moves far inward in the with-lithium case (red) compared to the pre-lithium profile (blue). The pre-lithium case uses conditional averaging of profiles in the last 50% of the ELM cycle of multiple discharges (like #129015) in a narrow density range. The profiles are typically flat or slightly hollow in the ELMy discharges. Indeed the profiles are very slowly evolving toward higher density, but the evolution between ELMs is fairly reproducible in a range of density, as taken here. In addition the profiles are typically flat or slightly hollow in the ELM-free discharges with lithium also. These profiles are clearly evolving, with density increasing with time. The particular fits are done over a 100 ms time window as described in the earlier articles [8, 23]. The gradient near to the edge in temperature profile remains unchanged but inside of 95% of ψ_N, a substantial change in gradient and increase of temperature are observed in figure 1(*b*). Another notable change occurs

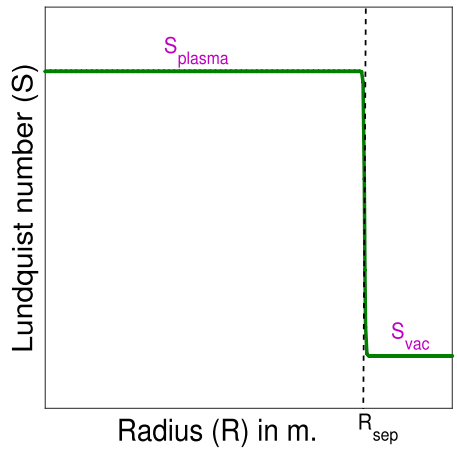

Figure 2. The profile of the Lundquist number with major radius used in the simulation is drawn here. The value of S_{plasma} and S_{vac} are varied to define the ideal limit of growth rate in ideal single- and two-fluid MHD model. R_{sep} is the position of the separatrix.

in the plasma current density profile as shown in figure 1(*c*). The highly peaked bootstrap region in edge current density in the pre-lithium case (blue line) becomes more widened in the with-lithium case. But, the safety factor profile (figure 1(*d*)) is almost unchanged.

3. Extended MHD equations and NIMROD Modelling of ELMs

The extended MHD equations used in our NIMROD calculations are:

$$\frac{\partial n}{\partial t} + \nabla \cdot (n\mathbf{u}) = 0 \tag{1}$$

$$mn\left(\frac{\partial}{\partial t} + \mathbf{u} \cdot \nabla\right)\mathbf{u} = \mathbf{J} \times \mathbf{B} - \nabla p - \nabla \cdot \overline{\overline{\Pi}} \tag{2}$$

$$\frac{3}{2}\left(\frac{\partial}{\partial t} + \mathbf{u}_\alpha \cdot \nabla\right)T_\alpha = -nT_\alpha \nabla \cdot \mathbf{u}_\alpha - \nabla \cdot \mathbf{q}_\alpha \qquad (\alpha = i, e) \tag{3}$$

$$\frac{\partial \mathbf{B}}{\partial t} = -\nabla \times \left[\eta \mathbf{J} - \mathbf{u} \times \mathbf{B} + \frac{1}{ne}\left(\mathbf{J} \times \mathbf{B} - \nabla p_e + \frac{m_e}{e}\frac{\partial \mathbf{J}}{\partial t}\right)\right] \tag{4}$$

$$\mu_0 \mathbf{J} = \nabla \times \mathbf{B}; \qquad \nabla \cdot \mathbf{B} = 0 \tag{5}$$

where $\mathbf{u}$ is the centre-of-mass flow velocity with particle density n and ion mass m, p is the combined pressure of electron (p_e) and ion (p_i), η represents resistivity, $\mathbf{q}_{e,i}$ denotes conductive heat flux vectors and $\overline{\overline{\Pi}}$ is the ion stress tensor including gyro-viscous components as described in the earlier reference [24, 25]. The initial-value NIMROD code has been consistently employed to study different ideal and non-ideal phenomena related to MHD space and time scales in both fusion and space plasma [26–30].

Unlike the true vacuum model (no particle, no current) used in eigenvalue ideal MHD codes such as ELITE, NIMROD uses a vacuum-like or halo region to model the free boundary modes. The halo region is designed as a low-temperature, low-density plasma compared to the high-density, high-temperature core plasma. The effective parameter for accurate modelling of the perfectly conducting ideal core plasma and infinitely resistive vacuum-like region is the Lundquist number, which is defined as $S = \tau_R/\tau_A$. Here, the resistive diffusion time $\tau_R = \mu_0 a^2/\eta$ (with μ_0 being the permeability of free space, η resistivity and a the minor radius) and the Alfven time scale $\tau_A = R_0\sqrt{\mu_0\rho_{m0}}/B_0$ (with R_0 being the major radius, B_0 the magnetic field and ρ_{m0} mass density at magnetic axis, respectively). As η approaches zero, S approaches infinity, which defines the ideal MHD limit of the resistive MHD model. Here, this limit was carefully obtained for the model of the vacuum-like halo region following previous articles on the benchmarking study using NIMROD, ELITE and GATO [26]. In our calculations, two different types of η profiles were employed: the realistic Spitzer resistivity model and the model hyperbolic tangent function centred at the separatrix (as shown in figure 2). In our simulation, both resistivity models are adopted to investigate the effect of η on the stability of the low-n peeling-ballooning modes, in order to explain the ELM suppression in NSTX Li-conditioned H-mode discharge. The numerical convergence is consistently checked in the following simulation and is shown in detail in the fifth section.

4. Pre-lithium case study in NIMROD

In this section, the results of our linear stability analysis of the NSTX ELMy reference discharge #129015 are described in detail. The stability of the peeling-ballooning modes was examined for both ideal single-fluid and two-fluid MHD, including the effects of the finite Larmor radius and diamagnetic drift. A step-like, hyperbolic tangent function for S (or η) profile was considered with a sharp transition from a high plasma value S_{plasma} to a low halo value S_{vac}. These two free parameters were adjusted separately to determine the growth rates of the low-n modes ($n = 1$–6) in the ideal single-fluid MHD limit. Note that the toroidal modes $n = 1$, 2 are found to be stable in the ideal single-fluid MHD model. Figure 3(*a*) shows the normalised growth rate versus the S_{plasma} graph for different n values over a wide S range (10^5–10^{10}). The lower and upper limits indicate a highly resistive plasma and a low η limit, respectively, compared with the experimental value in the pre-lithium case ($S_{\text{plasma}} \sim 4.92 \times 10^6$, considering the average $Z_{\text{eff}} = 2$). The growth rates of all modes remain almost unchanged above $S_{\text{plasma}} \sim 10^8$, which yields the value of the growth rate in the ideal single-fluid MHD limit. Also, the growth rate increases with increasing η, as found in previous simulation results [26, 31]. For the other limit, S_{plasma} was kept fixed at 10^{10}, and S_{vac} was varied from 10^2–10^5. The growth rates of all modes increased with the vacuum resistivity until saturation, as shown in figure 3(*b*). Thus, the results from the ideal single-fluid MHD analysis, predict excitation of the

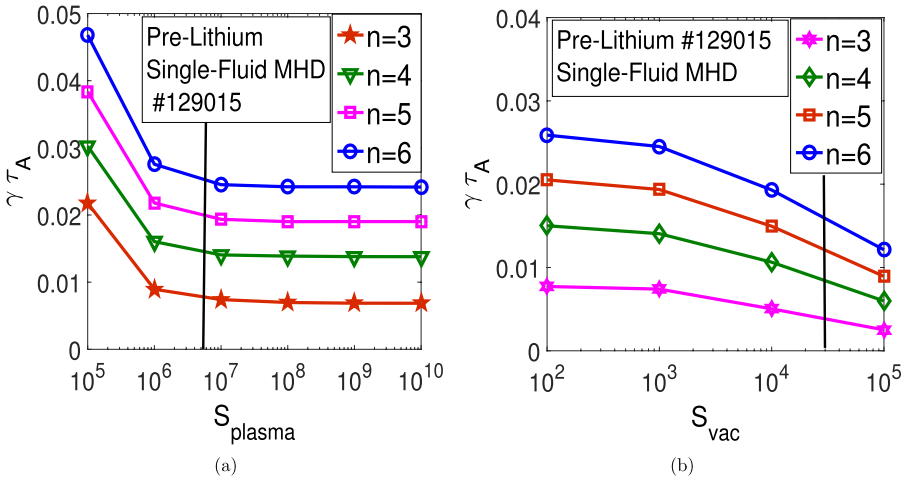

Figure 3. (*a*) Growth rates of modes $n = 3$–6 normalised with Alfven time versus plasma Lundquist number graph and (*b*) Variation of normalised growth rates of $n = 3$–6 with vacuum Lundquist number in ideal single-fluid MHD. Every mode reaches the ideal limit in the growth rate value around $S_{\text{plasma}} \sim 10^8$. With increasing resistivity (decreasing S_{plasma} and S_{vac}), all modes have further increments in growth rate. The experimental calculated value of the Lundquist number in the plasma and halo region is marked with a black line in each graph.

peeling-ballooning instability. But a different scenario occurs as the two-fluid effects become involved in the simulation. As shown in figure 4(*a*), the two-fluid effects further destabilise the $n = 3$, 4 modes and excite the $n = 2$ mode, which is stable in the ideal single-fluid MHD. The higher-mode growth rates ($n > 4$) are reduced compared to the ideal single-fluid MHD. A similar comparison of the growth rate versus different S_{plasma} values was preformed for the ideal two-fluid MHD model, as shown in figure 4(*b*). As in the case of the ideal single-fluid MHD, the ideal two-fluid MHD limit for the growth rates of modes $n = 2$–6 is found after the $S_{\text{plasma}} \sim 10^8$ value. Unlike the ideal single-fluid MHD model result, the growth rates of all modes in the two-fluid MHD model generally decrease with increasing η. This is an important finding in the context of NSTX ELM suppression, as explained below.

Next, we report the same qualitative trends for the results obtained after using the Spitzer resistivity model ($\eta(T_e) = \eta_0\, Z_{\text{eff}}(T_{e0}/T_e)^{3/2}$) in the calculation, where T_{e0}, η_0, Z_{eff}, and T_e denote the electron temperature, the resistivity at the magnetic axis, the effective charge number of all ions and the electron temperature profile, respectively. The resistivity is gradually enhanced by increasing Z_{eff}, similar to the experimental increase in Z_{eff} following Li coating. Here, our parameter space deviates from the ideal limit and lies in the resistive domain. The low-n modes ($n = 3$–5) becomes stabilized after a certain value of Z_{eff}; however, modes $n > 5$ become more unstable with increased Z_{eff} (figure 5). Therefore, the resistivity plays an influential role in the stability of the low-n kink/peeling modes in NSTX.

5. With-lithium case study in NIMROD

In this section, we discuss the possible mechanism found in NIMROD calculation behind NSTX ELM suppression. The procedure remains the same as that which is described in the previous section. First, the stability of the with-lithium discharge #129038 in the ideal two-fluid MHD model was checked, with all profiles being kept identical to the experimental profiles. In the ideal two-fluid MHD model, the with-lithium case exhibits two unstable modes ($n = 3$, 4) only, and all other modes are stabilised. Thus, the evident changes in the electron density, temperature and current density profiles stabilise all modes, except the two modes with $n = 3$, 4. We note that these two modes are also the fastest-growing modes in the discharge prior to the Li coating #129015. As shown in figure 6(*a*), both modes reach the growth rate value of the ideal two-fluid MHD limit above $S_{\text{plasma}} = 10^8$, where S_{vac} is fixed at 10^3. Then, if we reduce the value of S_{plasma} by enhancing η, the growth rates of $n = 3$, 4 gradually decrease. Finally, these modes become stabilised at much higher η, where S is two orders of magnitude lower than the actual experimental range of S ($\sim 10^7$) if the effects from increasing Z_{eff} is not considered. Otherwise, if S_{vac} is gradually decreased while the value of S_{plasma} remains fixed at 10^8, the growth rates of both modes initially decrease slightly. Then, at a significantly lower S in vacuum, the $n = 4$ mode continues to grow slowly and mode $n = 3$ become even more unstable (as shown in figure 6(*b*)). This result suggests that the plasma η has the main influential effect on the stabilisation of all modes, not the η in the halo region. In a real experimental scenario, the halo-region η maintains a finite value, because of the presence of partially ionised plasma with low density and temperature. The purpose of this analysis will be clarified when we discuss the results obtained using the Spitzer resistivity profile in the next paragraph. For the pair values of $S_{\text{plasma}}/S_{\text{vac}} \sim 10^{10}/10^3$, a comparison between the ideal single-fluid MHD and two-fluid MHD results is shown in figure 7(*a*). The trend is similar to the pre-lithium case shown in the previous section, as all modes ($n = 2$–6) are unstable in the ideal single-fluid MHD, even after using the Li-conditioned profiles. When the two-fluid effects are incorporated, all modes except $n = 3$, 4 become stabilised. But the growth rates of these two modes become higher than those in the ideal single fluid MHD.

Next, we clarify our new finding of resistive stabilisation of low-n modes in NSTX. The ideal two-fluid MHD analysis

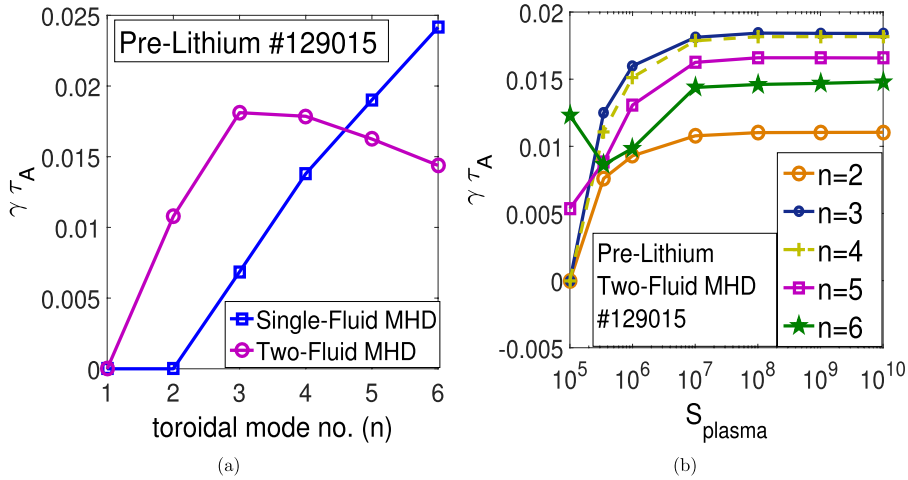

Figure 4. (*a*) Normalised growth rates of modes $n = 1$–6 versus toroidal mode number graph for both ideal single-fluid and two-fluid MHD. Two-fluid effects are found to destabilise the low-n modes and stabilise the high-n modes. Mode $n = 2$ becomes unstable only in the ideal two-fluid MHD. (*b*) Variation of normalised growth rate of $n = 2$–6 with the plasma Lundquist number in the two-fluid MHD of pre-lithium case. With decreased S_{plasma}, a gradual reduction in the growth rate is found for the $n = 2$–5 modes. But, the $n = 6$ mode becomes more unstable at a higher resistivity value.

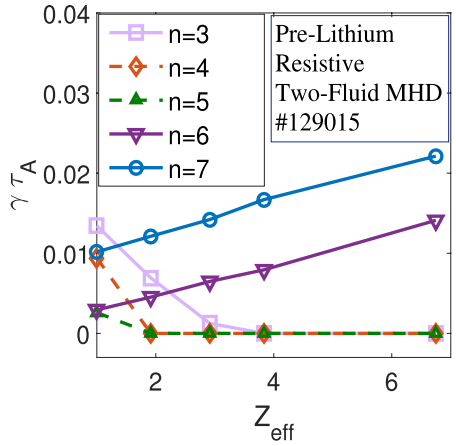

Figure 5. This figure contains the result of the normalized growth rate of modes $n = 3$–7 versus Z_{eff} in resistive two-fluid MHD (Spitzer resistivity) study of pre-lithium discharge. With the increase in average Z_{eff} value, the growth rate of low-n modes (3–5) decreases and at a higher value of Z_{eff}, they become stabilized. However, high-n modes such as (6, 7) become more unstable with increasing Z_{eff} value.

has shown that the profile changes are unable to provide complete stabilisation of the ELMs in the with-lithium case. Using the Spitzer resistivity profile and keeping all other profiles the same as NSTX experimental ones, the modes $n = 3$, 4 are found still growing at $Z_{\text{eff}} = 1$ as shown in figure 7(*b*). The contour plots of different perturbed quantities such as temperature, velocity and magnetic field of mode $n = 4$ are shown in figure 8. The mode structures confirm the edge localized nature of the dominant instabilities identified in our calculations, i.e. they are not core modes. In other words, the remnant unstable $n = 3$, 4 modes remain to be edge-localized that correspond to the ELMs observed in the NSTX experiment. It was observed in the experiment that the values of Z_{eff} increased during the process of ELM suppression. Similarly, when we increase the average value of Z_{eff} in the Spitzer resistivity expression, the growth rates of modes $n = 3$, 4 gradually decrease, as shown in figure 7(*b*). Note that an increase in Z_{eff} can increase collisionality at the edge pedestal region, which increases η and, accordingly, decreases the bootstrap current. As direct experimental profiles are employed in this study, the modification of the current density is automatically incorporated, as described in section 2. Thus, a more complete representation of the with-lithium case in numerical modelling, can be achieved if we include the enhanced value of Z_{eff}, as measured in the experiment, in the 3.5 ($\psi_N = 0.9$) to 4.0 ($\psi_N = 0.7$) range [8].

We check the numerical convergence in our simulation, including the radial and poloidal grid points, the time-step size, and the polynomial degree of the basis of finite elements used in the NIMROD calculations. Figures 9(*a*) and (*b*) show that the growth rates of the $n = 3$, 4 modes remain unchanged for $\delta t = 8 \times 10^{-9}$–$5 \times 10^{-9}$ s, and poloidal grid numbers in the range 250–300. Therefore, this numerical simulation converges well in terms of the δt size and the poloidal grid points. Figure 9(*c*) shows the variation of the growth rates of $n = 3$, 4 with Z_{eff} for polynomial degrees of both 5 and 6, and both curves are closely coincident; thus, they are well converged. As shown in figure 9(*d*), the growth rate with radial grid points is slightly varying but the error is within a reasonable limit.

6. Comparison of pre-lithium and with-lithium analyses

We propose that the resistive stabilisation on the low-n ELMs is a general finding for NSTX H-mode discharge, as this behaviour has been found in both the pre- and with-lithium cases. In the ideal two-fluid limit, the fastest growing modes

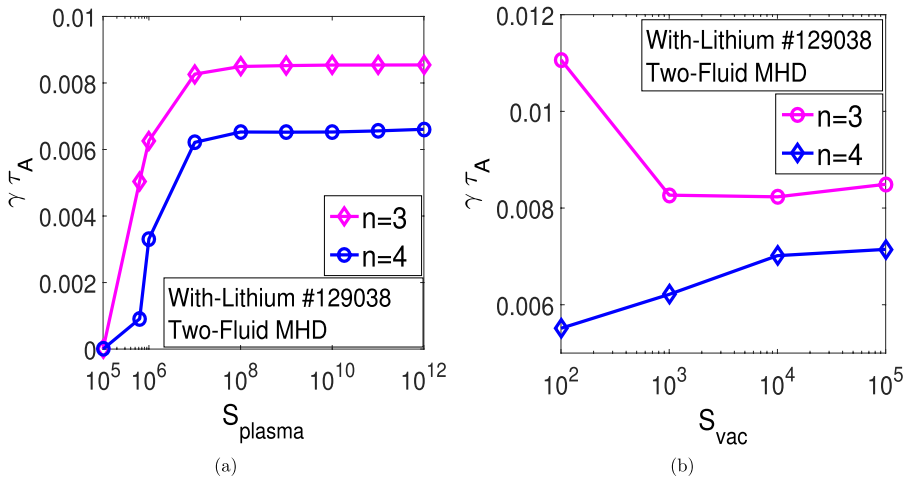

Figure 6. Normalised growth rate of modes $n = 3, 4$ versus (*a*) plasma Lundquist number and (*b*) vacuum Lundquist number for with-lithium discharge in two-fluid MHD model. The growth rate of $n = 3, 4$ reaches ideal limiting value around $S_{\text{plasma}} \sim 10^8$. The growth rate of $n = 3, 4$ decreases with decreased S_{plasma}. With decreased S_{vac}, $n = 4$ always remains slowly growing but $n = 3$ becomes more unstable.

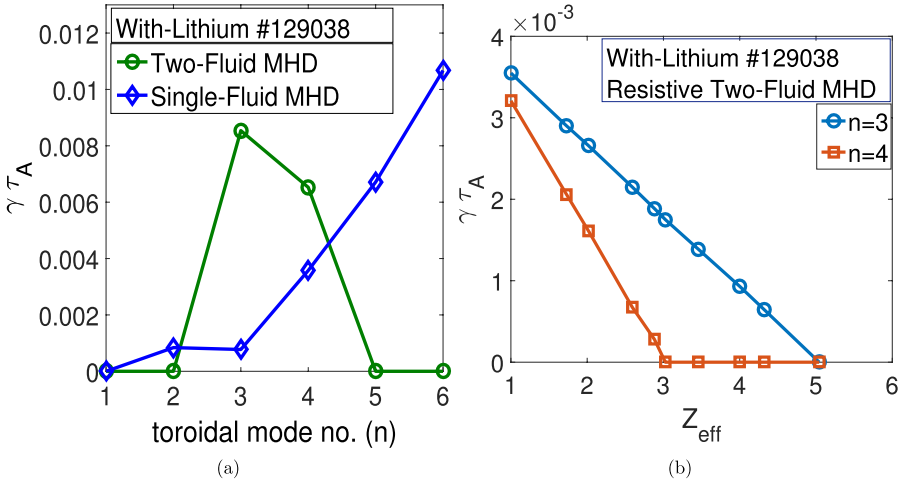

Figure 7. (*a*) Normalised growth rate of modes $n = 1$–6 versus toroidal mode number for both ideal single- and two-fluid MHD. Excluding $n = 3, 4$, all other modes become stabilised in two-fluid MHD model. (*b*) Normalised growth rate versus Z_{eff} for modes $n = 3, 4$ in resistive two-fluid MHD (Spitzer resistivity) study of with-lithium case. The remaining unstable $n = 3, 4$ modes at $Z_{\text{eff}} = 1$ become completely stabilised at approximately $Z_{\text{eff}} = 5$ and $Z_{\text{eff}} = 3$, respectively.

are $n = 3, 4$, for both the pre- and with-lithium coatings discharges. This finding does agree with the results from earlier analyses using the ELITE and PEST eigenvalue codes [7]. For the with-lithium case, all modes are stabilised in the ideal two-fluid MHD model, except $n = 3, 4$. In the pre-lithium ELMy H-mode, all modes except $n = 1$ are unstable; however, modes $n > 4$ have reduced growth rates when the two-fluid effects are included. After the increased η is considered by increasing Z_{eff}, ELM stabilisation is found for both cases in the resistive two-fluid MHD model for the low-n modes, i.e. $n = 3$–5. However, modes higher than $n = 5$ become more unstable with increased η in the pre-lithium case, but not for the with-lithium case. In both cases, this stabilization is only achieved in the two-fluid resistive MHD model. For purely resistive MHD model without two-fluid effects, the increase in η always destabilizes all ranges of ELMs. This contrasts to the recent study using NIMROD, where the resistive stabilising effects on low-n edge localized modes appear in the single-fluid MHD models [27], which might be arising from different resistivity models used.

Different resistivity profiles have been considered to understand the role of pedestal resistivity profile on linear growth rate of ELMs. For step-like hyperbolic tangent resistivity profile used in sections 4 and 5, the higher uniform value of η in plasma is found to lower the growth rate. In a more realistic situation, the use of the Spitzer profile with the same higher η value provides better stabilization than the step-like resistivity case. So, we presume that besides η value, the profile of resisitivity at the pedestal region also has an influential effect on the ELM growth rate. Next, we investigate why, in

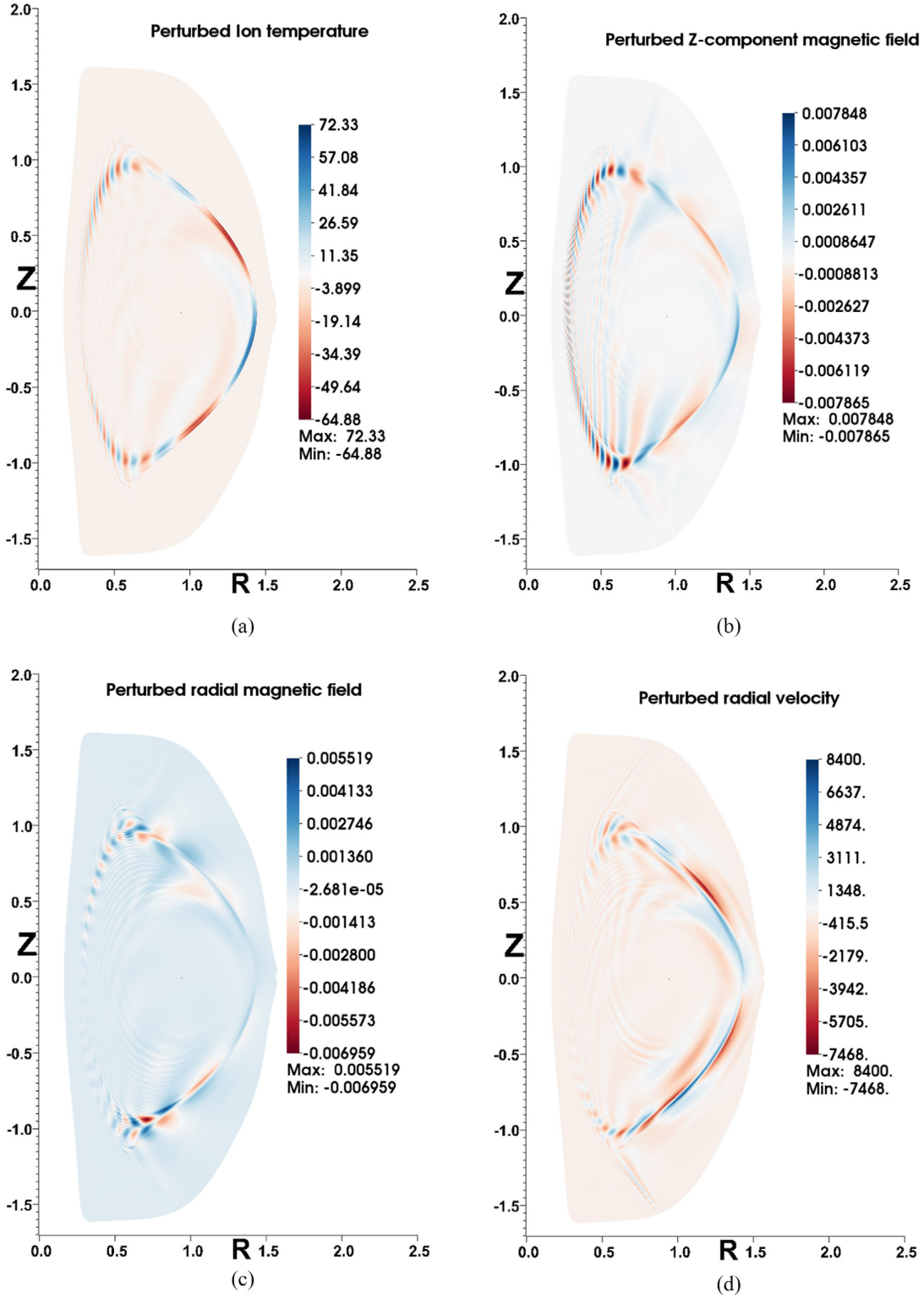

Figure 8. (With-Lithium discharge #129038) Contour plots of perturbed quantities $T_i(a)$, $B_z(b)$, $B_r(c)$ and $u_r(d)$ for $n = 4$ mode for the with-lithium case. The mode structures confirm the edge localized nature of the dominant instabilities identified in our calculations, i.e. they are not core modes.

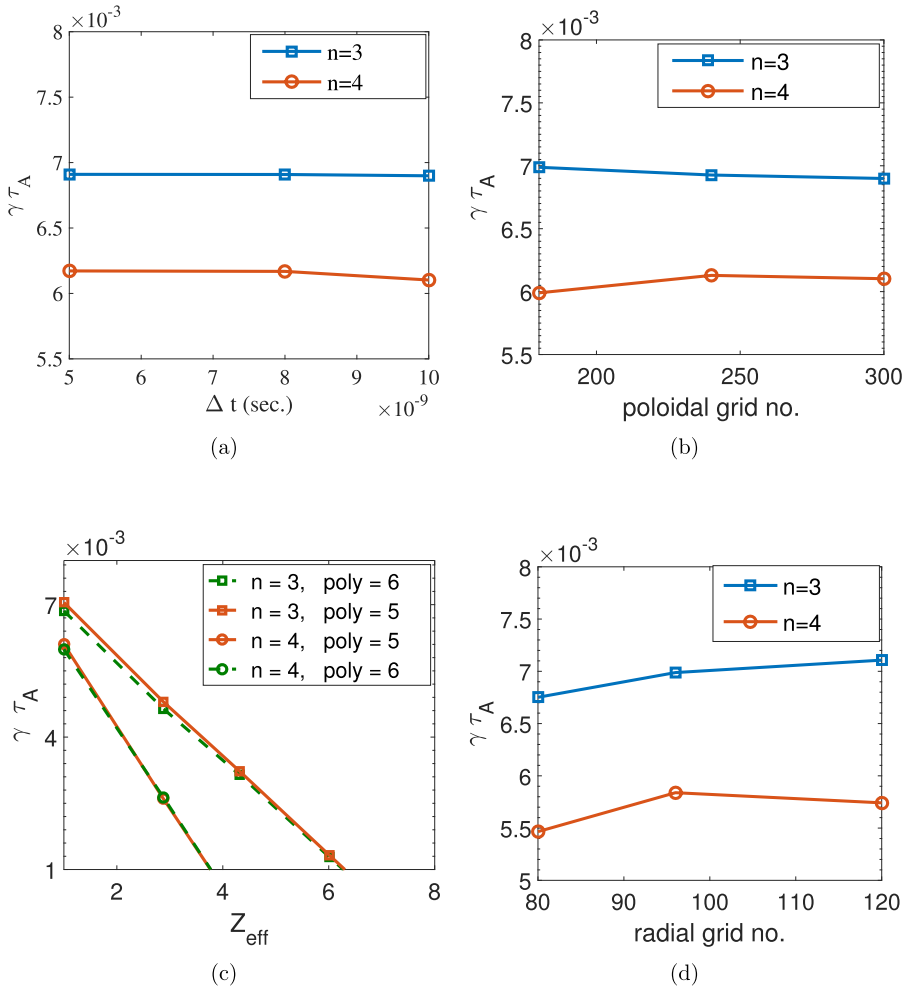

Figure 9. (With-Lithium discharge #129038) Linear growth rates for $n = 3$, 4 modes as a function of numerical parameters such as time step (*a*), numbers of grid points in the azimuthal direction (*b*) and radial direction (*d*) and Z_{eff} of different polynomial degree of finite elements (*c*) used in NIMROD calculations. Numerical convergence of our simulation has been demonstrated in these figures.

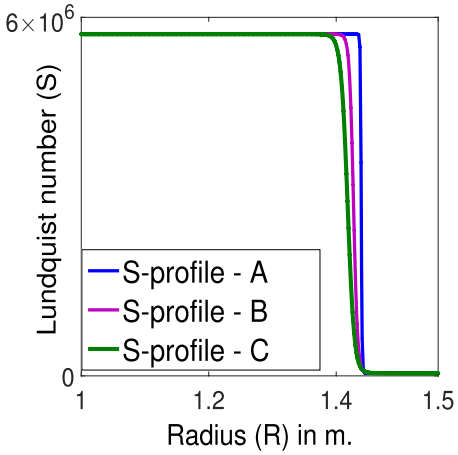

Figure 10. Different Lundquist number profiles with major radius used to study the resistivity profile effect on growth rate of ELMs. These are formed after varying the slope of an hyperbolic tangent function centered at the separatrix. Profile-A with the high steep gradient is close to the step-like profile; profile-C with less gradient than profile-B, has variation in resistivity value over the entire pedestal.

previous sections, Spitzer resistivity profile has led to better stabilization than using the step-like profile. This analysis has been performed in two ways—at first step, a comparison of results from Spitzer and step-like profiles is made for same pair of values of S_{plasma} and S_{vac}; in second step, the results from hyperbolic tangent resistivity profile for three different slopes at the pedestal region (as shown in figure 10) are compared. In the figure 11(*a*), the normalized growth rates of $n = 3$, 4 with step-like profile of η (profile-A in figure 10), are plotted for different values of S_{plasma}. We have found that even after decreasing S_{plasma} (increasing resistivity) to the same value of the stabilising level of Z_{eff} ($\sim$4) as in the Spitzer resistivity case (figure 7(*b*)), the stabilization is significantly weaker for profile-A than the Spitzer resisitivity case shown in figure 7(*b*). This analysis indicates that in addition to the value, the profile of resistvity at the pedestal region is equally influential on ELMs growth rate. In the second step, we have separately employed three Lundquist number profiles having different gradients at the pedestal as shown in figure 10. The profile-A is close to the step-like profile and profile-C is less steep than profile-B. Next, using the same values of $S_{\mathrm{plasma}}/S_{\mathrm{vac}}$

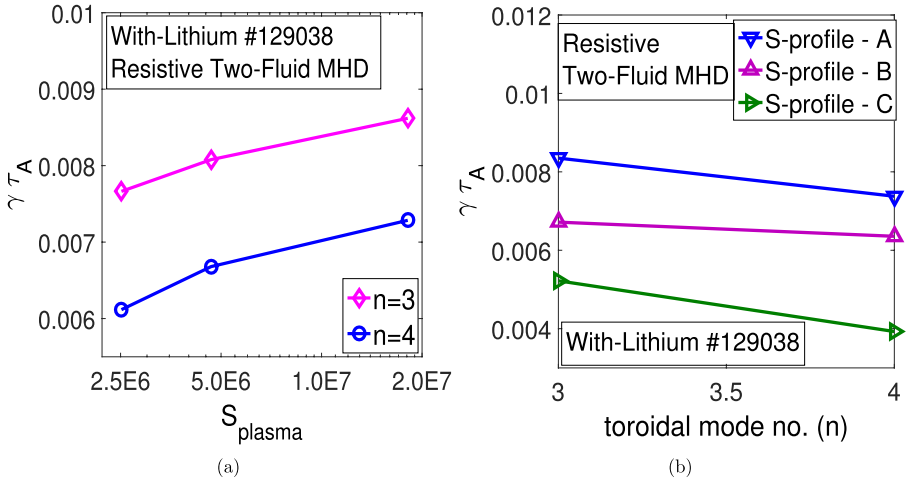

Figure 11. (*a*) Normalised growth rate versus plasma Lundquist number for modes $n = 3, 4$ using profile A. The maximum and minimum values of S_{plasma} are associated with the average Z_{eff} values of 1 and 4, respectively. After increasing Z_{eff} from 1 to 4, the reduction in growth rate is much weaker than Spitzer profile case (figure 7(*b*)) (*b*) Normalised growth rate versus toroidal mode no. for different resistivity profiles (A, B, and C) in with-Lithium case. For the same level of $S_{\text{plasma}}/S_{\text{vac}}$ values, profile C has the strongest stabilising effect than the step-like profile A for both $n = 3$ and 4 modes.

for all three profiles-A, B and C, the growth rates of $n = 3, 4$ modes are calculated and shown in figure 11(*b*). It is clear that profile 'C', having variation of η in a wide region across the pedestal, provides better stabilization (37% more than profile-A for $n = 3$) than profiles A and B. This finding explains why the Spitzer resistivity profile provides better stabilization than the uniform resistivity case.

7. Discussion and summary

A study of NSTX experimental equilibria was conducted using the NIMROD code to investigate the stability of the linear peeling-ballooning modes after Li conditioning. A comparison between the pre-lithium ELMy discharge and with-lithium ELM-free discharge was shown for both the ideal and resistive regimes of resistive MHD model. Full extended MHD modelling, including the finite-Larmor radius ion gyro-viscosity, two-fluid Hall and electron diamagnetic drift effects, was employed in the simulation. For the with-lithium equilibrium, the profile modification was found to be responsible for suppressing the higher-n ($n > 4$) modes. However, the $n = 3, 4$ modes were found to remain unstable with the ELM structure in the ideal two-fluid MHD model. In the resistive regime, including the Spitzer resisitivity model with $Z_{\text{eff}} = 1$, the with-lithium case was also found to be unstable for $n = 3, 4$. When the enhanced η due to the increase in Z_{eff} was included, these modes became fully stabilised. This result provides a new explanation for the observed ELM suppression following Li conditioning in NSTX. Thus, the NIMROD results indicate that, in addition to the stabilising effect of profile modifications, the enhanced η plays a key role in explaining the mechanism behind complete ELM suppression in Li-conditioned H-mode discharge.

This newly found resistive stabilising effect may contribute to the complete physical mechanism underlying the Li-induced ELM suppression through a virtuous cycle; that is, the initial refinement in the electron pressure profile following reduction of the divertor recycling induces an initial reduction in the ELM frequency and size, yielding increased Z_{eff} due to impurity accumulation at the edge pedestal. The enhancement in Z_{eff} introduces additional resistive stabilisation of the low-n ELMs, which in turn reinforce the impurity accumulation and the resulting Z_{eff} enhancement until complete ELM suppression is obtained.

This study of non-ideal effects on the stability of ideal MHD ELMs is expected to be applicable to impurity-conditioned experiments in other tokamaks. In recent ELM-free Li-coated discharge in EAST, the increased Z_{eff} may have been responsible for exciting edge harmonic oscillations in the ELM-suppression process. Thus, consideration of the important effect of Z_{eff}, during the design of future reactor-like machines such as ITER, CFETR would be worthwhile.

Acknowledgments

The research was supported by the National Magnetic Confinement Fusion Program of China under Grant Nos. 2014GB124002, 2015GB101004, and the 100 Talent Program of the Chinese Academy of Sciences (CAS). Author D. B. is partially supported by CAS President International Fellowship Initiative (PIFI), the China Postdoctoral Science Foundation Grant No. 2016M592054 and the Anhui Provincial Natural Science Foundation Grant No. 1708085QA22. Author P. Zhu also acknowledges the supports from U.S. DOE grant Nos. DE-FG02-86ER53218 and DE-FC02-08ER54975. We are grateful for the support from the NIMROD team. The numerical calculations in this paper have been done on the super computing system in the Supercomputing Center of University of Science and Technology of China. This research used resources of the National Energy Research Scientific Computing Center, a DOE Office of Science User Facility

supported by the Office of Science of the U.S. Department of Energy under Contract No. DE-AC02-05CH11231. The experiment in NSTX was supported by DOE under Contract No. DE-AC02-09CH11466. The digital data for this paper is available at http://arks.princeton.edu/ark:/88435/dsp018p58pg29j.

References

[1] Kinsey J.E. *et al* 2011 *Nucl. Fusion* **51** 083001
[2] Connor J.W., Hastie R.J. and Taylor J.B. 2004 *Plasma Phys. Control. Fusion* **46** B1
[3] Lortz D. 1975 *Nucl. Fusion* **15** 49
[4] Snyder P.B. *et al* 2007 *Nucl. Fusion* **47** 961
[5] Loarte A. *et al* 2007 Progress in the ITER physics basis chapter 4: power and particle control *Nucl. Fusion* **47** S203
[6] Chan V.S. *et al* 2015 *Nucl. Fusion* **55** 023017
[7] Maingi R. *et al* 2009 *Phys. Rev. Lett.* **103** 075001
[8] Maingi R. *et al* 2012 *Nucl. Fusion* **52** 083001
[9] Hu J.S. *et al* 2015 *Phys. Rev. Lett.* **114** 055001
[10] Osborne T.H. *et al* 2015 *Nucl. Fusion* **55** 063018
[11] Maggi R. *et al* 2016 *Nucl. Fusion* **55** 113031
[12] Bortolon A. *et al* 2016 *Nucl. Fusion* **56** 056008
[13] Boyle D.P. *et al* 2011 *Plasma Phys. Control. Fusion* **53** 105011
[14] Banerjee D., Zhu P. and Maingi R. 2017 *Phys. Plasmas* **24** 054501
[15] Maingi R. *et al* 2010 *Phys. Rev. Lett.* **105** 135004
[16] Bell M.G. *et al* 2006 *Nucl. Fusion* **46**
[17] Maingi R. *et al* 2005 *Nucl. Fusion* **45** 1066
[18] Maingi R. *et al* 2005 *Nucl. Fusion* **45** 264
[19] Snyder P.B. and Wilson H.R. 2004 *Plasma Phys. Control. Fusion* **46** A131
[20] Bell M.G. *et al* 2009 *Plasma Phys. Control. Fusion* **51** 124054
[21] Scotti F. *et al* 2013 *Nucl. Fusion* **53** 083001
[22] Canik J.M. *et al* 2013 *Nucl. Fusion* **53** 113016
[23] Canik J.M. *et al* 2011 *Phys. Plasmas* **18** 056118
[24] Sovinec C.R., Glasser A. and the NIMROD Team 2004 *J. Comput. Phys.* **195** 355
[25] Sovinec C.R., King J.R. and the NIMROD Team 2010 *J. Comput. Phys.* **229** 5803
[26] Burke B.J. *et al* 2010 *Phys. Plasmas* **17** 032103
[27] King J.R. *et al* 2016 *Phys. Plasmas* **23** 062123
[28] Zhu P. and Raeder J. 2013 *Phys. Rev. Lett.* **110** 235005
[29] Ebrahimi F. and Raman R. 2015 *Phys. Rev. Lett.* **114** 205003
[30] Izzo V.A. *et al* 2015 *Nucl. Fusion* **55** 073032
[31] Ferraro N.M., Jardin S.C. and Snyder P.B. 2010 *Phys. Plasmas* **17** 102508